

# Twin-assisted cracking degradation in sodium layered oxide cathodes

**Cheng Chen**

Central South University

**Zhen Han**

Nanjing University

**Chaoping Liang**

Central South University <https://orcid.org/0000-0002-2910-2938>

**Yiming Feng**

Central South University

**Peng Wang**

Nanjing University <https://orcid.org/0000-0003-0788-6687>

**Weifeng Wei** (✉ [weifengwei@csu.edu.cn](mailto:weifengwei@csu.edu.cn))

Central South University <https://orcid.org/0000-0002-3088-6549>

---

## Article

**Keywords:** twinning, sodium layered oxides, crystallographic defects

**Posted Date:** March 18th, 2021

**DOI:** <https://doi.org/10.21203/rs.3.rs-290193/v1>

**License:**   This work is licensed under a Creative Commons Attribution 4.0 International License.

[Read Full License](#)

---

# Abstract

Twinning defects often present in crystalline materials when are subject to mechanical stimuli and are mostly affecting their physicochemical properties. The twinning formation and twin-related degradation upon cycling in sodium layered oxides (SLOs) are poorly understood. Combining atomic-resolution imaging, spectroscopy and first principles calculations, we reveal that growth twinning is unexpectedly common in the SLO materials and the twin boundaries show distinct structural and chemical characters from those identified in lithium layered oxides. A unique O-P-O twinning plane was identified in the O3 type SLO materials. We discover that twin-assisted Na diffusion cause large volume variations and trigger intragranular fracture during electrochemical cycling. The present findings not only establish a robust correlation between growth twinning and intragranular cracking in SLOs, but also offer general implications for the development of high-performing intercalation electrode materials by regulating crystallographic defects.

## Main Text

Twinning formation and dislocation slip are two main deformation modes for nearly all the crystalline solids as their response to external applied load or internal thermal stress<sup>1</sup>. In addition to the majority of these mechanical phenomena that are observed in metallic materials<sup>2,3</sup>, recent years have witnessed increasing interests on these mechanical behaviors in transition metal layered oxides upon electrochemical cycling<sup>4-12</sup>, given their widespread application as cathode materials in Li- and Na-ion rechargeable batteries. Thereinto, the dislocation generation and dynamics have been well correlated with the structural degradations such as phase transition and mechanical cracking in lithium layered oxides when cycled in high voltages<sup>4-8</sup>, accounting mostly for their voltage fade and capacity loss. Hence it is intuitive to ask whether or not the twinning planar defects would play an analogous role in the electrochemical performance of layered oxide cathodes.

Thus far few studies have focused on theoretical and experimental analyses on how the twinning defects form and how the twin interfaces affect the electrochemical kinetics of alkali metal ions in common  $\text{LiCoO}_2$ <sup>9-11</sup> and  $\text{NaMnO}_2$  layered oxides<sup>12</sup>. Specifically, coherent twin boundaries (CTBs) can form in pristine epitaxial-grown single-crystal  $\text{LiCoO}_2$  film<sup>9,10</sup>, and these twin boundaries detrimentally affect the redox voltages and Li ion transportation on the basis of experimental results and first principles calculations<sup>9,10</sup>. Nevertheless, CTBs and related structural degradation are still not well understood for sodium layered oxides at atomic scale, with only one study mentioning the observation of multiple twinning and briefly discussing the impact on the electrochemical kinetics of  $\text{Na}^+$  in layered  $\text{NaMnO}_2$ <sup>12</sup>. Here combining high angle annular dark field- and annular bright field-scanning transmission electron microscopy (STEM-HAADF/-ABF), 4D-STEM techniques<sup>13-16</sup> and first principles calculations<sup>1</sup>, we demonstrate that the CTB with a (003) preferred orientation is a common planar defect in sodium layered oxides and twin boundaries exhibit distinct structure and chemistry from the bulk structure. Specifically, these CTB facilitate fast diffusion of Na ions and cause significant expansion of interslab space and

induce intragranular fracture along boundaries, which plays an unforeseen influence on the structural integrity and electrochemical performance during extended cycling.

We choose Ni-based  $\text{NaNi}_{0.5}\text{Co}_{0.2}\text{Mn}_{0.3}\text{O}_2$  (NNCM) compound because of its high theoretical capacity and elemental availability<sup>17-19</sup>. More importantly, both Ni and Mn exhibit strong Jahn-Teller activity associated with the  $e_g$  electrons of Ni(III) and Mn(III)<sup>20</sup>, which may bring about lattice distortions and trigger the formation of CTB defects. Spherical NNCM compound aggregates in micron size were synthesized through coprecipitation plus solid-state calcination processes (Extended Data Fig. 1), as reported in our previous studies<sup>21,22</sup>. The XRD pattern for the pristine NNCM is indexed as typical O3-type  $R\bar{3}(\_)m$  phase, and this layered structure is well maintained after electrochemical cycling (Extended Data Fig. 2). However, drastic variations in voltage curves and reversible capacities are noticeable in the NNCM cathode between the first and subsequent cycles (Extended Data Figs. 3-4), the negligible average structure evolution observed in Extended Data Fig. 2 can hardly account for the rapid voltage decay and capacity fading. Intuitively, local structural and chemistry changes occurred in the cycled NNCM cathode would be expected.

Fig. 1 shows the cross-sectional structure of the cycled NNCM cathode after 10 cycles. Intragranular cracks, including straight-through cracks that follow a strict crystallographic preference along the (003) plane (Fig. 1a) and zigzag cracks or stair-like cracks that propagate in zigzags connecting two straight lines (Fig. 1d), are detectable in the cycled NNCM particles. Intragranular cracking is well recognized to be a main contributor to performance degradation of layered oxide cathodes since new cathode–electrolyte interfaces are generated, which gives rise to undesirable surface reconstruction and TM ion dissolution, excessive electrolyte consumption and deteriorated electronic conductivity<sup>7,23-24</sup>. Hence, a better understanding of the origin and propagation of intragranular cracks is crucial to optimize sodium layered oxide cathodes. Interestingly, the atomic-resolution STEM-HAADF images and corresponding fast Fourier transform (FFT) pattern (Fig. 1b-c) show that the straight-through crack coincides exactly with a CTB, which can be identified from the diffraction pattern as a (003) plane and the  $[1(\_)00]$  and  $[100]$  zone axes for the two adjacent grains forming the twin boundary. Fig. 1d-f show that two parallel CTB join together by plane  $(01(\_)2(\_))$ , resulting in a novel zigzag crack. An antiphase boundary (APB) also emerges along the zigzag crack, and there are extended cracks and material loss around APB, as shown in Fig. 1f. The observations confirm that the twin boundaries are the key factor that induces intragranular cracks in the cycled NNCM cathode.

The above STEM analysis reveals the CTB-related cracking degradation in the cycled NNCM cathode, but some fundamental questions concerning the origin of CTB behavior are still unanswered: 1) How the CTBs form, through growth twinning during materials process or deformation twinning upon electrochemical cycling? 2) Are there any local variations in crystal and electronic structures along or away from the twin-boundary interface? 3) What is the driving force for the preferential crack nucleation and propagation along the CTB? To unravel these questions, we employ simultaneous STEM-HAADF, STEM-ABF and 4D-STEM imaging, electron energy loss spectroscopy (EELS) and theoretical calculations

to study the CTB in as-synthesized NNCM material. As shown in Extended Data Figs. 5a-b, representative HAADF and corresponding reconstructed color maps confirm that multiple CTBs along [001] direction, sharing a common (003) plane are prevalent planar defects in as-synthesized NNCM. The atomic-resolution HAADF images (Extended Data Figs. 5c-e) indicate that all the multiple CTBs strictly adhere to the [1(−)00] and [100] zone axes, implying that CTBs generate through growth twinning during materials process.

To explore the local structural and chemical variations along and away from the twin boundary, geometry phase analysis (GPA) based on STEM imaging and EELS analysis were also carried out. Figs. 2a-c show the STEM-HAADF/-ABF and corresponding GPA results. It is apparent from the STEM-ABF image (Fig. 2b) that the CTB exhibits much brighter contrast than other regions, which infers that Na deficiency occurs along boundary. The EELS spectra taken from the CTB and adjacent twin-crystals are compared in Extended Data Fig. 6. Apparently, no noticeable chemical shifts could be observed for the *L*-edges of TM ions, but the enlarged energy difference between pre-edge peak and main peak for oxygen suggests the lower Na occupancy of the twin boundary<sup>25</sup>. The internal strain  $\varepsilon_{yy}$  mapping calculated by GPA (Fig. 2c) displays the internal strain distribution along (003) plane relative to the CTB. Interestingly, uneven fluctuations on internal strain are evident, showing the largest tensile strain along the CTB and repeating oscillations between tensile and compressive strains every 8-10 atomic layers. The tendency in the internal strain distribution is ascribed to the changes in the TM-O interlayer spacing (or local elastic distortions), which can be explicable mostly by the long-range electrostatic interactions and/or van der Waals effects<sup>25</sup>. Moreover, based on the close-up HAADF image and line-profile (Fig. 2d-e), the largest interlayer space and the lowest atomic contrast are detectable along the CTB, and the  $\text{NaO}_6$  configuration deviates from the octahedral geometry for typical O-type structure apparently, showing a typical prismatic shape that is common in the P-type layered structure. A clear consensus has been established that P-type layered oxides are generally Na-deficient when compared with their Na-stoichiometric O-type counterparts<sup>26</sup>, which may explain the Na deficiency observed in the CTBs.

Considering that Na and O ions are virtually invisible in the STEM-HAADF image and the interpretation of STEM-ABF image is difficult due to its complicated contrast transfer function (CTF)<sup>15</sup>, the center of mass (COM) imaging technique<sup>16</sup> which is one of 4D-STEM imaging techniques was implemented to imaging the novel CTBs structure using the pixelated detector, and all reconstructed images including phase reconstructed (COM related) images are shown in Extended Data Fig. 7. Note that the integrated COM (iCOM) and differential COM (dCOM) images clearly observe all the TM, Na and O atoms, which are rather different from the HAADF and ABF images, so the atomistic configuration of CTBs and contiguous areas can be visualized precisely. Evidently from the dCOM images in Figs. 3a-b, the O-Na arrangement follows the prismatic geometry, and the contrast of Na ions is also much weaker in the CTB, when compared with that in the O3-type structure. The enlarged interspacing and less Na occupancy associated with the P-type CTB are well consistent with the well-recognized differences between O- and P-type layered structures<sup>26</sup>.

To appreciate the CTB formation and its potential impacts on electrochemical kinetics and structure integrity, density-functional-theory (DFT) calculations within the GGA + U framework were performed<sup>27,28</sup>. The optimized O3 structure and twin structure are shown in Extended Data Fig. 8, and the O-P-O twin configuration is in good agreement with the experimentally detected structure. The calculated total energies (Fig. 3c) show that O3 structure is the ground-state phase at  $x = 0$  of  $\text{Na}_{1-x}[\text{NCM523}]\text{O}_2$ , P2 structure is the most unstable phase, while the twin structure has an energy in-between O3 and P2 structure. At  $x = 0.25$ , the P2 becomes the most stable phase, the O-P-O twin still in-between phase while O3 is the least stable phase. The intermediate total energy of O-P-O twin indicates the O-P-O twin structure is likely to form while the synthesis condition deviated the pure O3 or P2 phase zone.

As the interlayer distance of P2 phase is larger than O3 phase, the developed internal strain would be expected as evidenced in the GPA analysis of Fig. 2c. The simulated GPA results (Fig. 3d) from the calculated O-P-O twin structure present similar modulated periodic pattern, i. e., the twin layer has larger positive strain while the O layer has negative strain due to the long-range cooperative Coulombic interactions between  $\text{TMO}_2$  slabs. The calculated charge density difference (Extended Data Fig. 9) is also in good agreement with the dDPC-STEM image (Fig. 3b). From the calculated charge density of  $x=0$  of  $\text{Na}_{1-x}[\text{NCM523}]\text{O}_2$ , the TM ions lose more electrons and accordingly oxygen ions get more electrons on the P layer, which build a strong electrostatic repulsion near the P twin layer (Fig. 4a). The desodiation could alleviate this repulsion and reduce the built-in strain field. As shown in the calculated charge density difference of  $x = 0.25$  (Fig. 4a), the loss of electrons of TM ions and the gain of electrons of oxygen ions are respectively less than those of  $x = 0$ .

To understand how this charge density distribution influences the electrochemical properties and the stability of layered structure, the voltage profile and Na diffusion barriers are calculated. The Na diffusion barrier for P2 is also lower than that for O3 phase (Extended Data Fig. 10). The lower voltage and diffusion barrier indicate that the desodiation will preferentially happen on the O-P-O twin layer. Even though it could reduce the electrostatic repulsion, the preferential desodiation on the O-P-O twin layer results in the collapse of the layered structure. As shown in Fig. 4b, the interlayer distance of the O-P-O twin layers increases sharply during desodiation. The excessive expansion of O-P-O twin layers cause the crack generation and propagation within the SLO particles, when compared with the common O3 structure (Figs. 4c-d). Together with the poor air and moist stability of layered sodium structure<sup>29,30</sup>, the intragranular cracks will soon develop and lead to rapid electrochemical degradation of SLO cathode materials.

In summary, we have identified the growth coherent twinning with a (003) preferred orientation as a common planar defect in sodium layered oxides. We find that in contrast to the octahedral geometry for O3-type structure,  $\text{NaO}_6$  at the twin interface shows a typical prismatic configuration with Na-deficiency feature. The O-P-O twin structure brings about uneven fluctuations on internal strain and assists Na diffusion (or preferential desodiation) along the twin boundary, which lead to large interslab expansion and crack initiation at the end of charge and in turn bring forth fast capacity loss and voltage fading of

SLO cathode during extended cycles. Atomic-scale experimental observations and DFT results are well consistent to provide evidence in the physical origin of the stability of the O-P-O twin structure and the correlation between twin and cracking. The better understanding of twin-assisted structural degradation in SLO cathodes here may have general implications for emphasizing the important role that structural defects play in determining electrochemical properties of intercalation electrode materials.

## References

1. Hull, D. *Introduction to Dislocations*. (Butterworth-Heinemann. Press, 2011).
2. Greer, J. R. & De Hosson, J. T. M. Plasticity in small-sized metallic systems: Intrinsic versus extrinsic size effect. *Prog. Mater. Sci.* **56**, 654-724 (2011).
3. Zhu, Y. T., Liao, X. Z. & Wu, X. L. Deformation twinning in nanocrystalline materials. *Prog. Mater. Sci.* **57**, 1-62 (2012).
4. Wang, H., Jang, Y. I. & Huang, B., Sadoway, D.R. & Chiang, Y.T. TEM study of electrochemical cycling-induced damage and disorder in LiCoO<sub>2</sub> cathodes for rechargeable lithium batteries. *J. Electrochem. Soc.* **146**, 473-480 (1999).
5. Gabrisch, H., Yazami, R. & Fultz, B. The character of dislocations in LiCoO<sub>2</sub>. *Electrochem. Solid-State Lett.* **5**, A111-A114 (2002).
6. Ulvestad, A. *et al.* Topological defect dynamics in operando battery nanoparticles. *Science* **348**, 1344-1347 (2015).
7. Yan, P. *et al.* Intragranular cracking as a critical barrier for high-voltage usage of layer-structured cathode for lithium-ion batteries. *Nat. Commun.* **8**, (2017).
8. Singer, A. *et al.* Nucleation of dislocations and their dynamics in layered oxide cathode materials during battery charging. *Nat. Energy* **3**, 641-647 (2018).
9. Moriwake, H. *et al.* First-Principles Calculations of Lithium-Ion Migration at a Coherent Grain Boundary in a Cathode Material, LiCoO<sub>2</sub>. *Adv. Mater.* **25**, 618-622 (2013).
10. Jiang, Y.Y. *et al.* Atomistic mechanism of cracking degradation at twin boundary of LiCoO<sub>2</sub>. *Nano Energy* **78**, (2020).
11. Gong, Y. *et al.* In Situ Atomic-Scale Observation of Electrochemical Delithiation Induced Structure Evolution of LiCoO<sub>2</sub> Cathode in a Working All-Solid-State Battery. *J. Am. Chem. Soc.* **139**, 4274-4277 (2017).
12. Abakumov, A.M., Tsirlin, A.A., Bakaimi, I., Van Tendeloo, G. & Lippas, A. Multiple Twinning As a Structure Directing Mechanism in Layered Rock-Salt-Type Oxides: NaMnO<sub>2</sub> Polymorphism, Redox Potentials, and Magnetism. *Chem. Mater.* **26**, 3306-3315 (2014).
13. Lohr, M. *et al.* Differential phase contrast 2.0-Opening new "fields" for an established technique. *Ultramicroscopy* **117**, 7-14 (2012).

14. Shibata, N. *et al.* Differential phase-contrast microscopy at atomic resolution. *Nat. Phys.* **8**, 611-615 (2012).
15. Lazic, I., Bosch, E. & Lazar, S. Phase contrast STEM for thin samples: Integrated differential phase contrast. *Ultramicroscopy* **160**, 265-280 (2016).
16. Mueller, K. *et al.* Measurement of atomic electric fields and charge densities from average momentum transfers using scanning transmission electron microscopy. *Ultramicroscopy* **178**, 62-80 (2017).
17. Han, M.H., Gonzalo, E., Singh, G. & Rojo, T. A comprehensive review of sodium layered oxides: powerful cathodes for Na-ion batteries. *Energy Environ. Sci.* **8**, 81-102 (2015).
18. Wang, P-F., You, Y., Yin, Y-X. & Guo, Y-G. An O3-type  $\text{NaNi}_{0.5}\text{Mn}_{0.5}\text{O}_2$  cathode for sodium-ion batteries with improved rate performance and cycling stability. *J. Mater. Chem. A* **4**, 17660-17664 (2016).
19. Nanba, Y. *et al.* Redox Potential Paradox in  $\text{Na}_x\text{MO}_2$  for Sodium-Ion Battery Cathodes. *Chem. Mater.* **28**, 1058-1065 (2016).
20. Li, X. *et al.* Jahn–Teller Assisted Na Diffusion for High Performance Na Ion Batteries. *Chem. Mater.* **28**, 6575-6583 (2016).
21. Cheng, C. *et al.* Electrochemical Property-Structure Correlation for Ni-Based Layered Na-Ion Cathodes. *ACS Appl. Mater. Interfaces.* **10**, 28719-28725 (2018).
22. Cheng, C. *et al.* Unraveling Atomically Irreversible Cation Migration in Sodium Layered Oxide Cathodes. *J. Phys. Chem. Lett.* **11**, 5464-5470 (2020).
23. Yan, P., Zheng, J., Zhang, J.G. & Wang, C. Atomic Resolution Structural and Chemical Imaging Revealing the Sequential Migration of Ni, Co, and Mn upon the Battery Cycling of Layered Cathode. *Nano Lett* **17**, 3946-3951 (2017).
24. Mu, L. *et al.* Deciphering the Cathode-Electrolyte Interfacial Chemistry in Sodium Layered Cathode Materials. *Adv. Energy Mater.* **8**, (2018).
25. de Boisse B. M. *et al.* Coulombic self-ordering upon charging a large-capacity layered cathode material for rechargeable batteries. *Nat. Commun.* **10**, (2019).
26. Berthelot, R., Carlier, D. & Delmas, C. Electrochemical investigation of the  $\text{P2-Na}_x\text{CoO}_2$  phase diagram. *Nat. Mater.* **10**, 74-80 (2011).
27. Perdew, J.P., Burke, K. & Ernzerhof, M. Generalized gradient approximation made simple. *Phys. Rev. Lett.* **77**, 3865-3868 (1996).
28. Wang, L., Beach, KSD. & Sandvik, AW. High-precision finite-size scaling analysis of the quantum-critical point of  $S=1/2$  Heisenberg antiferromagnetic bilayers. *Phys Rev B* **73**, (2006).
29. Lu, Z. & Dahn, JR. Intercalation of Water in P2, T2 and O2 Structure  $\text{A}_z[\text{Co}_x\text{Ni}_{1/3-x}\text{Mn}_{2/3}]\text{O}_2$ . *Chem. Mater.* **13**, 1252-1257 (2001).
30. You, Y., Dolocan, A., Li, W. & Manthiram, A. Understanding the Air-Exposure Degradation Chemistry at Nanoscale of Layered Oxide Cathodes for Sodium-Ion Batteries. *Nano Lett.* **19**, 182-188 (2019).

## Methods

**Material synthesis.**  $\text{Ni}_{0.5}\text{Mn}_{0.3}\text{Co}_{0.2}\text{CO}_3$  precursors were synthesized by co-precipitation method. Specifically, an aqueous solution (2.0 M) was prepared by dissolving  $\text{NiSO}_4 \cdot 6\text{H}_2\text{O}$ ,  $\text{CoSO}_4 \cdot 7\text{H}_2\text{O}$  and  $\text{MnSO}_4 \cdot \text{H}_2\text{O}$  (the molar ratio of Ni : Co : Mn = 0.5: 0.2: 0.3) into deionized water, and then pumped into a continuously stirred tank reactor (CSTR). A 2 M  $\text{Na}_2\text{CO}_3$  solution was added to make the PH value around 7.8 while a 0.24 M  $\text{NH}_4\text{OH}$  solution was also slowly fed into the CSTR. The obtained precursors were filtered, washed with distilled water and then dried at 120 °C.  $\text{NaNi}_{0.5}\text{Co}_{0.2}\text{Mn}_{0.3}\text{O}_2$  material was prepared by mixing stoichiometric amounts of  $\text{Ni}_{0.5}\text{Mn}_{0.3}\text{Co}_{0.2}\text{CO}_3$  and NaOH, and then calcining at 850 °C for 10 h in flowing  $\text{O}_2$ , followed by by regrinding and calcination at 850 °C for 10 h again.

**Material characterizations.** Powder X-ray diffraction (PXRD) measurements were conducted on a D8 Bruker Advance diffractometer equipped with Cu K $\alpha$  radiation source ( $\lambda=1.54056 \text{ \AA}$ ). The obtained XRD patterns were refined on the basis of Rietveld method using GSAS-EXPGUI software<sup>31</sup>. The morphology of as-prepared material was investigated using field-emission scanning electron microscopy (FESEM, FEI). For scanning transmission electron microscopy (STEM) characterization, all cathode materials were thinned as TEM specimens with the traditional lift-out method by focus ion beam (FIB, Helios NanoLab 600i) process at 2 to 30 kV. STEM images were acquired on an aberration-corrected STEM Titan<sup>3</sup> G2 60-300 cubed with a field emission gun at 300 kV. Electron energy loss spectroscopy (EELS) spectra were acquired on a Gatan Quantum 966 system. In geometrical phase analysis (GPA) calculation process, vectors  $g [003]^*$  was selected<sup>32</sup>, and the spatial resolution is 1.5 nm and a mask with an accuracy of about 0.2% was utilized during fast Fourier transformation. 4D STEM data sets were acquired using an electron microscope pixel array detector (EMPAD) with a 128 $\times$ 128 pixel array at 1,100 frames per second<sup>33</sup>.

**Electrochemical measurements.** The active material, super P and polyvinylidene fluoride (PVDF) binder (the weight ratio = 0.8: 0.1: 0.1) were mixed in N-methyl-2-pyrrolidone (NMP). Then the resulting slurry was applied to an Al foil, and then dried at 110 °C for 12 h in a vacuum oven. The loading density of the active material was about 1.5-2.0 mg cm<sup>-2</sup>. The electrolyte was prepared by dissolving 1.0 M  $\text{NaClO}_4$  in propylene carbonate (PC) with 5 vol.% fluoroethylene carbonate (FEC). The CR2016 coin-type half-cell was fabricated by using a glass fiber to separate Na metal anode from working electrode in an Ar-filled glove box. Galvanostatic charge-discharge measurements were carried out using a LANHE-CT2001A battery testing system between 1.5 V and 4.0 V at room temperature. Cyclic voltammetry (CV) curves were measured with an Arbin electrochemical workstation (BT2000) with a scan rate of 0.1 mV s<sup>-1</sup> at room temperature.

**First principles calculation.** The DFT calculations are conducted on the Vienna ab initio simulation package (VASP)<sup>34</sup>, using plane-wave basis sets of the projector-augmented wave (PAW) method<sup>35</sup>. Generalized gradient approximation (GGA) of Perdew *et al.*<sup>27</sup> was adopted to describe the exchange and correlation interactions. The Hubbard U correction (DFT + U) was used to correct the self-interaction error

of TM<sup>27,28</sup>. U values of 6.8, 5.9, and 5.2 eV, as used by one of the authors in his previous work<sup>36-38</sup>, were chosen for Ni, Co, and Mn ions, respectively. We use the cutoff energies of 520 eV and 750 eV for the plane-wave basis and the augmentation charge, respectively. Gamma-center smearing method was used for the k space integration. The Na<sub>32</sub>[Ni<sub>16</sub>Co<sub>8</sub>Mn<sub>8</sub>]O<sub>2</sub> supercell adopted for present study contains 32 formula units of NaTMO<sub>2</sub>, which is mimic to the actual Na[Ni<sub>0.5</sub>Co<sub>0.2</sub>Mn<sub>0.3</sub>]O<sub>2</sub> synthesized in this work. An 8-layers structure is constructed to model the O-P-O twin structure, in which each layer contains 4 formula units of NaTMO<sub>2</sub>. 2 Ni, 1 Mn and 1 Co atoms are located in each layer of the supercell. The same TM ions distribution was used for the calculation of pure O3 and P2 phases. Climbing image nudged elastic band (CI-NEB) method was adopted to calculate the diffusion barrier for Na ions. An equivalently optimized k-point mesh was used to guarantee the same density per unit volume of the reciprocal lattice, and to ensure a convergence of 1 meV per unit cell. Periodic boundary conditions in three directions were added in all the calculations. The energy convergence criteria for the electronic and ionic relaxations were 0.01 meV and -0.02 eV/Å, respectively, while those the self-consistent static calculations were 0.01 meV. We considered spin-polarized magnetic configurations for all the calculations.

## References

31. Toby, B.H. EXPGUI, a graphical user interface for GSAS. *J. Appl. Cryst.* **34**, 210-213 (2001).
32. Rouviere, J.L. & Sarigiannidou, E. Theoretical discussions on the geometrical phase analysis. *Ultramicroscopy* **106**, 1–17 (2005).
33. Tate, M.W. *et al.* High Dynamic Range Pixel Array Detector for Scanning Transmission Electron Microscopy. *Microsc Microanal* **22**, 237-249 (2016).
34. Kresse, G. & Hafner, J. Ab Initio Molecular Dynamics for Liquid Metals. *Phys. Rev. B* **47**, 558-561 (1993).
35. Kresse, G. & Joubert, D. From Ultrasoft Pseudopotentials to the Projector Augmented-Wave Method. *Phys Rev B* **59**, 1758-1775 (1999).
36. Liang, C. *et al.* Unraveling the Origin of Instability in Ni-Rich LiNi<sub>1-2x</sub>Co<sub>x</sub>Mn<sub>x</sub>O<sub>2</sub> (NCM) Cathode Materials. *J. Phys. Chem. C* **120**, 6383-6393 (2016).
37. Liang, C. *et al.* Obstacles toward unity efficiency of LiNi<sub>1-2x</sub>Co<sub>x</sub>Mn<sub>x</sub>O<sub>2</sub> (x=0 similar to 1/3) (NCM) cathode materials: Insights from ab initio calculations. *J. Power. Sources.* **340**, 217-228 (2017).
38. Liang, C. *et al.* Site-dependent multicomponent doping strategy for Ni-rich LiNi<sub>1-2y</sub>Co<sub>y</sub>Mn<sub>y</sub>O<sub>2</sub> (y=1/12) cathode materials for Li-ion batteries. *J. Mater. Chem. A* **5**, 25303-25313 (2017).

## Declarations

### Acknowledgements

This work was supported by the National Natural Science Foundation of China (51304248, 11874199 and 51971250), the National Key Research and Development Program of China (Grant No.

2018YFB010400), SAFEA: High-End Foreign Experts Project (Grant No. B06020), Hunan Provincial Natural Science Foundation of China (2020JJ5733). The International Cooperation and Exchange Program by NSFC (11911530174). The Fundamental Research Funds for the Central Universities (020514380224). The Innovation Program of Central South University (2016CXS003), Open Project (621011913) the State Key Laboratory of Powder Metallurgy at Central South University.

### **Author contributions**

W.F.W. and P.W. conceived the idea and supervised all aspects of the research. C.C. performed the synthesis, XRD analysis and electrochemical measurements of all samples. Z.H., C.C. and P.W. performed the STEM measurements and analyzed the STEM results. C.P.L. and Y.M.F. carried out the theory calculations. W.F.W. and C.P.L. co-wrote the manuscript and all authors discussed the results and made comments on the manuscript.

### **Competing interests**

The authors declare no competing interests.

### **Additional information**

**Supplementary information** is available for this paper.

**Correspondence and requests** for materials should be addressed to W.F.W. or P.W.

## **Figures**

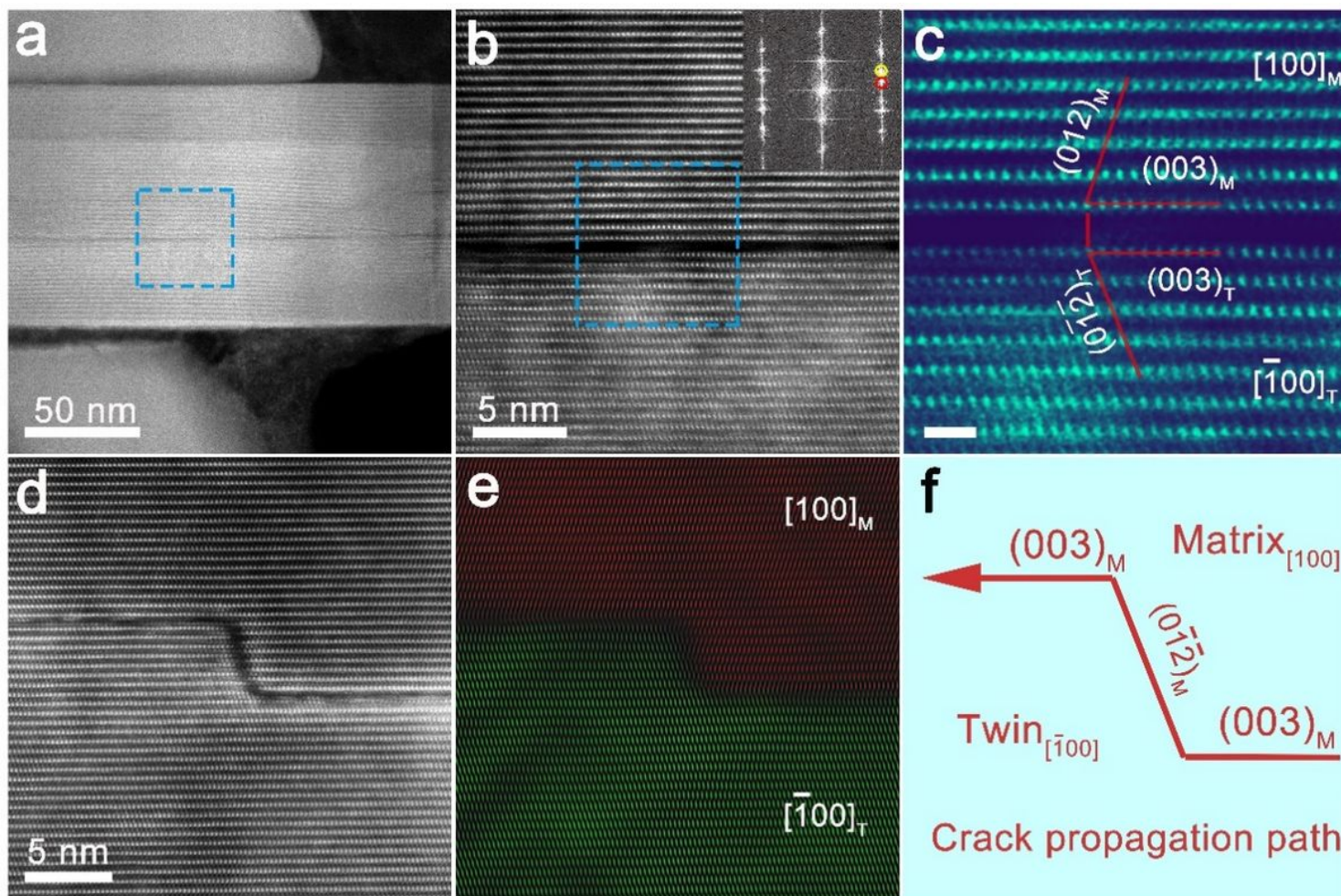


**Figure 1**

Intragranular cracking driven by twin boundaries in cycled NNCM cathode. (a-b) STEM-HAADF images of NNCM cathode after 10 cycles. (c) Atomic resolution STEM-HAADF images acquired from blue dashed rectangle in b (scale bar is 1 nm). (d-e) STEM-HAADF images and corresponding reconstructed images of cycled NNCM cathodes. (f) Schematic illustration of the crack propagation along CTB, demonstrating obvious preferred orientation of crack propagation.

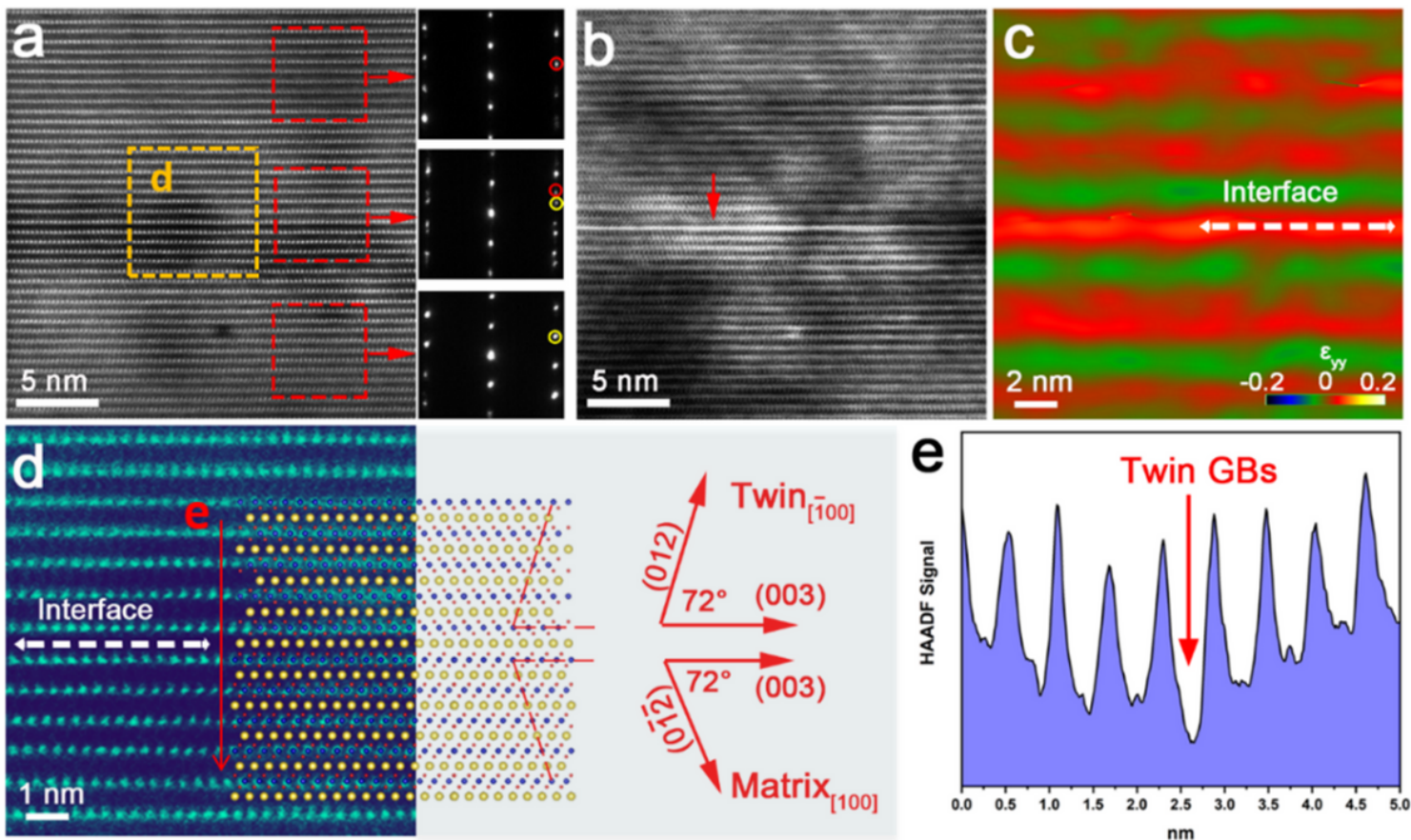
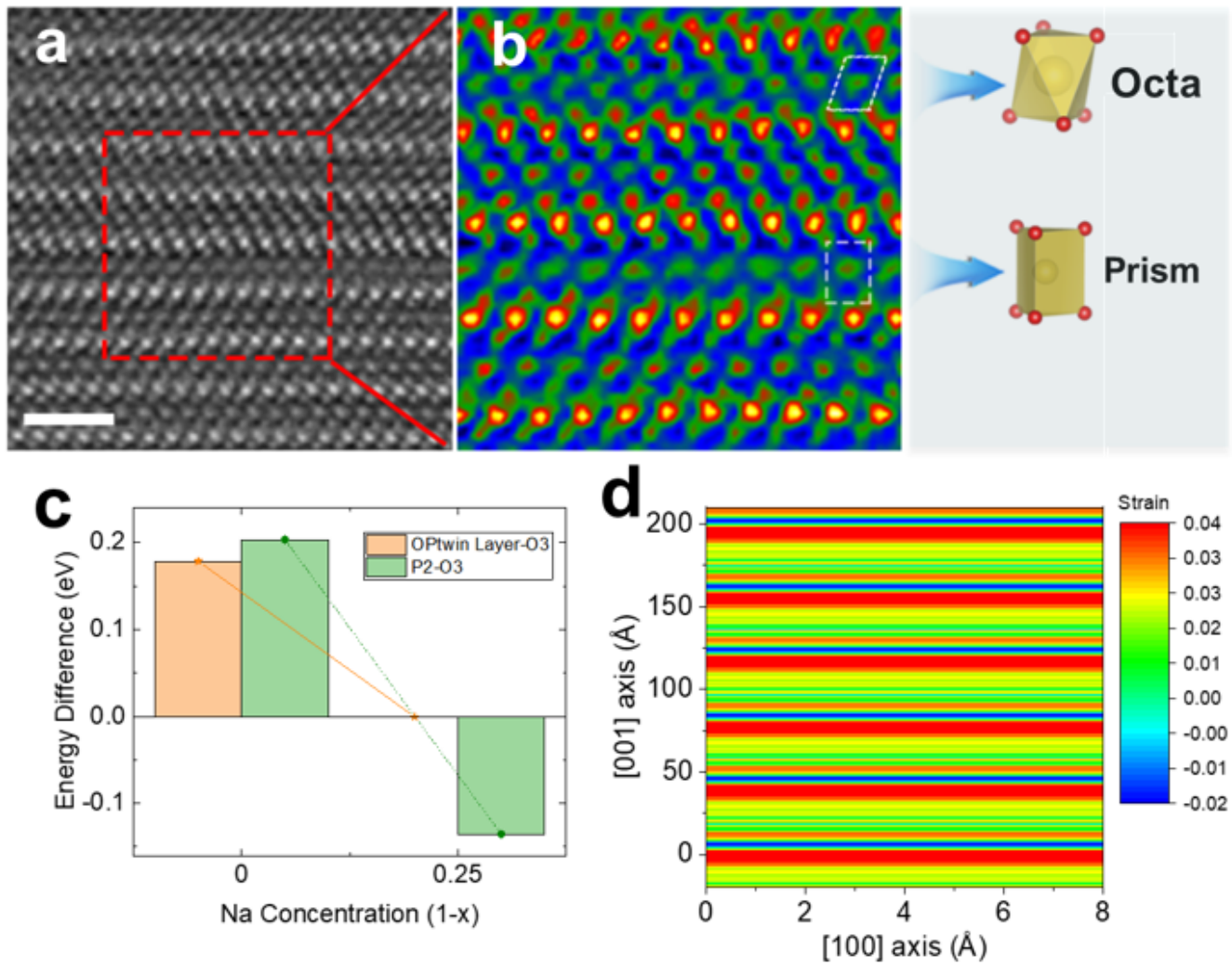


Figure 2

Atomic structural variations along and away from the twin boundary. STEM-HAADF (a) and ABF (b) images along  $[110]$  zone axis, corresponding FFT patterns acquired from the red-dashed rectangle. (c) The corresponding geometric phase analysis (GPA) patterns of NNCM cathodes. (d) Magnified image extracted from the orange-dashed rectangle of (a). (e) Intensity profile along the direction marked by the red arrow in d.



**Figure 3**

Atomic structure, charge density map and DFT results at the twin interface. (a) Atomic-resolution dCOM image of NNCM cathodes. Scale bar is 0.5 nm. (b) enlarged image of the selected area in (a). (c) Energy difference between the P2, OP-twin and O3 structure. (d) GPA patterns of NNCM cathodes obtained from DFT calculations.

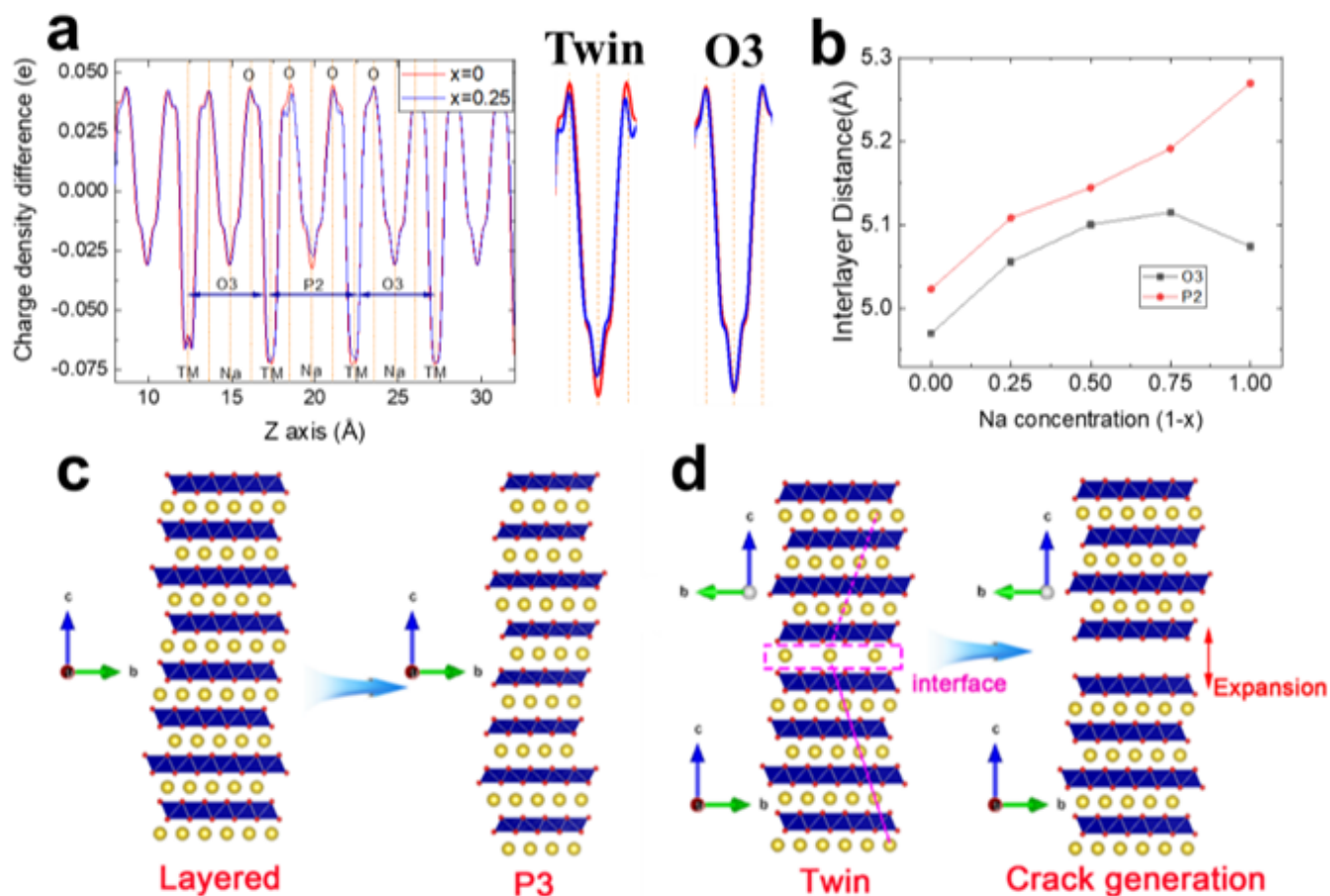


**Figure 4**

Calculated charge density difference, structural variation and crack generation mechanism at the twin interface. (a) Calculated charge density difference across the twin interface. (b) Calculated interlayer distance for P2 and O3 structures upon desodiation. (d-e) Schematic illustration of phase transition in twin-containing and O3 structure, demonstrating a novel degradation mechanism in layered NaTMO<sub>2</sub> oxides.

## Supplementary Files

This is a list of supplementary files associated with this preprint. Click to download.

- [SupplementaryInformation.docx](#)